ADVANCED ENERGY MATERIALS
www.advenergymat.de

Spatial Structure Engineering of Interactive Single Platinum Sites toward Enhanced Electrocatalytic Hydrogen Evolution

Chao Ye, Jieqiong Shan, Chongzhi Zhu, Wenjie Xu, Li Song, Yihan Zhu, Yao Zheng, and Shi-Zhang Qiao**

Regulating site-to-site interactions between active sites can effectively tailor the electrocatalytic behavior of single-atom catalysts (SACs). The conventional SACs suffer from low density of single atoms and lack of site-to-site interactions between them. Herein, a series of interactive Pt SACs with controllable Pt–Pt spatial correlation degree and local coordination environment is developed by integrating densely populated Pt single atoms in the sub-lattice of a Co_3O_4 matrix. The obtained interactive Pt-Co_3O_4 catalysts demonstrate remarkable electrocatalytic performance toward hydrogen production, outperforming those of isolated single atom- and nanoparticle-based catalysts. The intrinsic catalytic activity of interactive Pt-Co_3O_4 catalysts is closely dependent on the spatial structure of Pt sites with the adjusted *d*-band center by regulating contents and atomic configuration of Pt sites. This work provides fundamental insights for the structure-property relationship on interactive single active sites, which is expected to direct the rational design of highly efficient SACs.

1. Introduction

Reaction pathways and performance of heterogeneous catalytic processes are closely dependent on the atomic structure of catalysts.[1] Regulating atomic interactions between each pair of active sites is an intriguing strategy to optimize catalysts' properties.[2] Despite the high exposure of active sites, nanoparticle catalysts exhibit inflexible geometric structures with over-strong interatomic interactions, making the regulation of electronic and catalytic property difficult.[3] In contrast, single-atom catalysts (SACs) demonstrate precise atomic structure and simple spatial coordination, allowing an ideal platform to regulate site-to-site interactions between active sites.[4] However, conventional SACs feature low loading of active sites to ensure atomic dispersion, which leads to isolated active sites far away from one another. The long distance between active sites limits the formation of site-to-site interactions, thus results in lack of synergistic effect of active sites during the catalytic process.[5]

Recent studies in SACs have triggered significant research advances in investigating synergistic effect among individual single atoms mediated by well-designed geometric structures such as double-atom active sites,[6] single atom arrays,[7] topologically structured single atoms,[8] high-loading single atoms with reduced inter-site distance, etc.[9] All these so called "interactive SACs" have demonstrated enhanced catalytic performance in comparison with the conventional isolated SACs. Even though there has been a growing awareness of the significance of inter-site synergy between single atoms,[10] most of these developed catalysts exhibit random local coordination of single atoms, leading to an ambiguous mechanistic understanding of the impact of geometric structures on the catalytic performance.[11]

On the other hand, it remains a grand challenge to manipulate the electronic structure of single active sites continuously in a wide range with a controllable approach due to the insufficient regulation of site-to-site interactions. For example, as a widely studied electronic structure parameter, *d*-band centers of metal active sites have been applied to describe catalytic performance of nanostructured metal catalysts.[12] Although the *d*-band center of nanoparticle catalysts can be adjusted by various structure modification strategies including alloying, strain, etc., the continuous regulation of *d*-band center of single atoms has yet to be achieved in SACs.[13] So far, the continuous regulation of the atomic configuration and electronic structure is urgently required to establish a convinced structure-property relationship and promote the

C. Ye, J. Shan, Y. Zheng, S.-Z. Qiao
School of Chemical Engineering and Advanced Materials
The University of Adelaide
Adelaide SA5005, Australia
E-mail: yao.zheng01@adelaide.edu.au; s.qiao@adelaide.edu.au
C. Zhu, Y. Zhu
Center for Electron Microscopy
State Key Laboratory Breeding Base of Green Chemistry Synthesis Technology and College of Chemical Engineering
Zhejiang University of Technology
Hangzhou 310014, China
W. Xu, L. Song
National Synchrotron Radiation Laboratory
University of Science and Technology of China
Hefei 230029, China

The ORCID identification number(s) for the author(s) of this article can be found under https://doi.org/10.1002/aenm.202302190

DOI: 10.1002/aenm.202302190

substantial enhancement of catalytic performance of interactive SACs.

Herein, we developed a controllable approach to achieve a series of interactive Pt SACs with tunable site-to-site interactions and investigated the dependence of catalytic performance on the atomic configurations. Incorporated in the cationic sub-lattice of spinel oxide Co_3O_4, the spatial structure of Pt single atoms can be regulated by adjusting the content of Pt sites. The obtained Pt-Co_3O_4 (n) (n = 0.01, 0.04, 0.06, and 0.14) catalysts demonstrate continuously tunable Pt-Pt spatial correlation and local coordination to optimize their catalytic performance towards hydrogen evolution reaction (HER) in acidic environment. The optimal Pt-Co_3O_4 (0.06) catalyst demonstrates a remarkable HER specific activity with an exchange current density of 3.81 mA cm^{-2}_{Pt}, surpassing those of conventional isolated Pt SACs and nanoparticle Pt/C catalysts. Based on these interactive Pt SACs, we established the relationship between atomic configuration of Pt single atoms and the catalytic performance of corresponding catalysts. It is found that the catalytic property is governed by *d*-band center of active sites as manipulated by contents and atomic configurations of Pt sites. Therefore, this work opens a new pathway for rational design of interactive SACs with optimal catalytic performance.

2. Results and Discussion

2.1. Structure Characterizations of Pt-Co_3O_4 (n)

Based on an ion exchange-pyrolysis strategy that we reported previously,[14] we synthesized a series of Pt-incorporated Co_3O_4 catalysts with different contents of Pt substitutions (see Experimental Section for details). The obtained catalysts are denoted as Pt-Co_3O_4 (n), where n = 0.01, 0.04, 0.06, and 0.14 represents the Pt content in Co_3O_4 determined by inductively coupled plasma mass spectrometry (ICP-MS) (Table S1, Supporting Information). As illustrated in the X-ray diffraction (XRD) patterns (Figure S1, Supporting Information), all the Pt-Co_3O_4 (n) catalysts show the identical peaks of Co_3O_4 phase without Pt nanoparticles formed, suggesting that the Pt sites are accommodated in the Co_3O_4 lattice.[15] In addition, the Raman spectra of the Pt-Co_3O_4 (n) exhibit typical characteristic bands of Co_3O_4 with an observable redshift of the A_{1g} band, which confirms the well retention of spinel oxide and demonstrates the possible incorporation of Pt sites in the octahedral Co (Co_{oct}) sites (Figure S2, Supporting Information).[16]

2.2. Spatial Correlation Analyses of Pt-Co_3O_4 (n)

We performed detailed high-angle annular dark-field high-resolution scanning transmission electron microscopy (HAADF-HRSTEM) imaging and analysis to determine the spatial structure of Pt sites in various Pt-Co_3O_4 (n) catalysts. First, the HAADF-HRSTEM images of Pt-Co_3O_4 (n) catalysts evidently show that the integrated Pt sites with brighter contrast were uniformly distributed in the host lattice and become denser upon higher Pt contents (**Figure 1**a; Figure S3, Supporting Information). Atomic structure analysis have identified various doping configurations of the Pt sites, which are labelled with different colors (Figure S4, Supporting Information). In addition, the majority of Pt sites are identified at Co_{oct} sites for all Pt-Co_3O_4 (n) catalysts (Figure S5, Supporting Information). We then performed statistical analyses on a series of Pt-Co_3O_4 (n) catalysts to determine their spatial correlation's degree of Pt substitutions. Based on the labelling of a large amount of individual Pt sites (c.a. 7020 sites) in Pt-Co_3O_4 (n) catalysts, the partial projected pair distribution function (pPDF) profiles for <233> axe can be achieved (Figure 1b; Figures S6–S9, Supporting Information). Apparently, Pt-Co_3O_4 (0.01) catalyst exhibits a nearly flat pPDF profile with no correlation peak observed, indicating most Pt sites exist as isolated single atoms with random distribution. By contrast, the Pt-Co_3O_4 (0.04 – 0.14) catalysts exhibit gradually enhanced multiple correlation peaks with increase of Pt content. These peaks coincide well with the calculated pPDF histograms of the projected Co_{oct} cationic sublattice of Co_3O_4 along <233> direction, suggesting an increased spatial correlation of Pt sites identical to that of the host matrix.[8a] It should be noted that for Pt-Co_3O_4 (0.14) catalysts with elevated Pt concentration, some segregated Pt sites with distorted structures can be observed besides integrated Pt single sites, which broadens the correlation peaks of pPDF profiles. Such a trend in the degree of spatial correlation can be more vividly visualized in a topological view as shown in Figure 1c. Further, these labelled Pt sites are grouped into correlated Pt single atoms with different "clusters" sizes according to the maximum projected distance between Co_{oct} sites, the population and distribution of which can be evaluated and visualized (Figures S6–S9, Supporting Information). For the Pt-Co_3O_4 (n) catalysts with a higher Pt content, a larger population and mass fractions of correlated Pt sites (cluster size ≥ 2 atoms) is observed apart from isolated Pt sites (Figure S10, Supporting Information).

On the other hand, we conducted Pt L_3-edge X-ray absorption near-edge structure (XANES) and extended X-ray absorption fine structure (EXAFS) measurements to determine the valence state and local coordination of Pt substitutions in Co_3O_4. The Pt species in Pt-Co_3O_4 (n) catalysts show high valence states approaching that of the PtO_2 reference, demonstrating that the Pt sites are integrated into the lattcie rather than supported on the surface of Co_3O_4 (Figure S11, Supporting Information). As suggested by Co-K edge XANES and Fourier transform (FT)-EXAFS spectra, the Co species in the hybrid catalysts demonstrate similar valence state and coordination with the pure Co_3O_4, but decreased lattice symmetry has been induced by the incorporation of Pt single atoms into Co_3O_4 lattice (Figure S12, Supporting Information). The Pt L_3-edge FT-EXAFS spectra and the corresponding fitting results identified the existence of Pt-Pt second shell coordination in additon to Pt-Co_{oct} in the Pt-Co_3O_4 (n) catalysts, which is distinct from conventional isolated SACs (Figure 1d; Figure S13 and Table S2, Supporting Information). It is demonstrated that the coordination number (CN) of the second shell Pt–Pt scattering gradually increases with the increased Pt content in Pt-Co_3O_4 (n) catalysts, i.e., from 0.6 of Pt-Co_3O_4 (0.01) to 1.5 of Pt-Co_3O_4 (0.04), 2.0 of Pt-Co_3O_4 (0.06) and 2.3 of Pt-Co_3O_4 (0.14). This trend is in accordance with the percentage of correlated Pt single atoms as determined by HRTEM analysis, even though some Pt sites are segregated in Pt-Co_3O_4 (0.14), the majority of them exist as correlated single atoms. In addition, the CN of Pt-O coordination scatterings are ≈6.0, indicating that

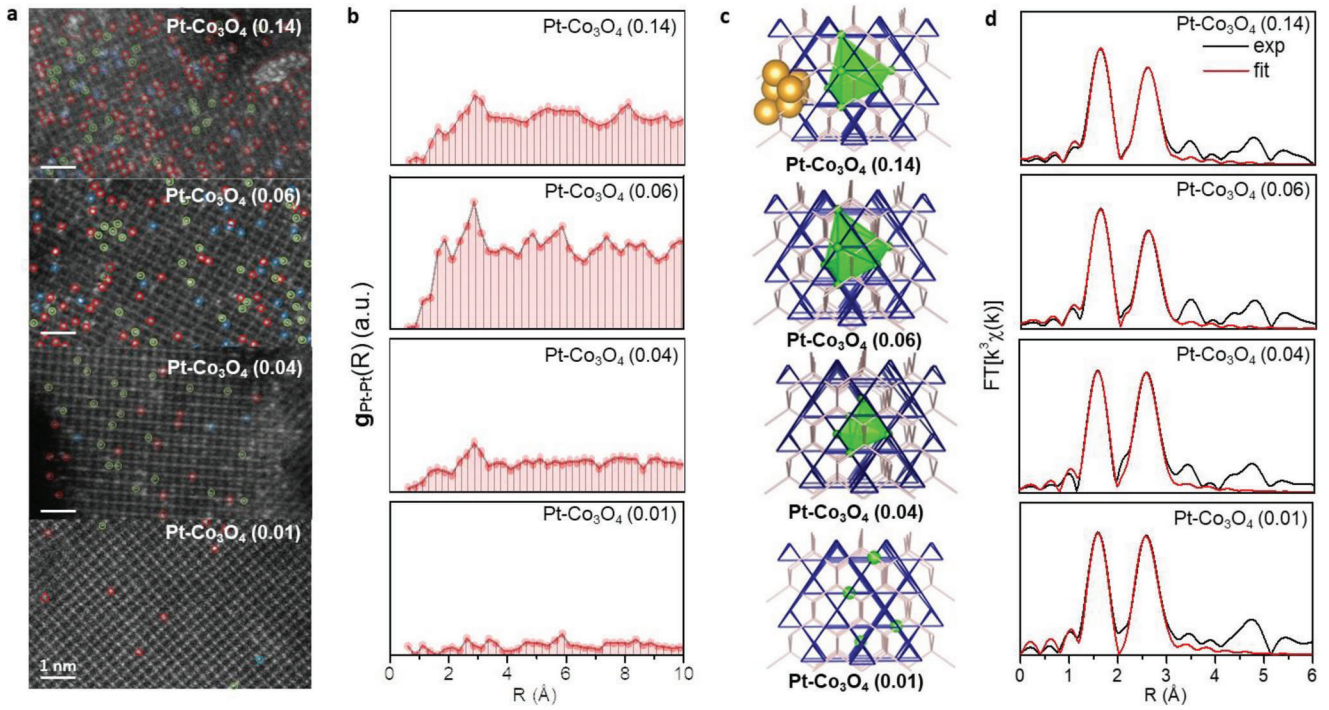

Figure 1. Spatial structure analyses of integrated Pt active sites. a) Atomic-resolution HRSTEM images of Pt-Co_3O_4 (n) catalysts along symmetry-related <233> direction. Pt atoms are labelled with various colors according to spatial structure of Pt substitutions as shown in Figure S4 (Supporting Information). b) Calculated projection-specific pPDF profiles for Pt-Co_3O_4 (n) catalysts based on the statistical analysis of Pt sites labeled in HAADF-HRSTEM images along <233> projection. c) The corresponding topological illustrations of Pt-Co_3O_4 (n) catalysts. The green polyhedron schematically illustrates the correlated substitution of Pt sites at the octahedral cationic sites. d) k_3-weighted FT-EXAFS Pt-L_3 edge experimental and fitting spectra of Pt-Co_3O_4 (n) catalysts.

Pt sites are the center of octahedron, which confirms their location in the lattice of Co_3O_4. It is therefore demonstrated that the spatial structure of Pt single atoms in Pt-Co_3O_4 (n) catalysts can be regulated in both spatial correlation and local coordination, which are mediated by the density of incorporated Pt sites within the lattice of Co_3O_4.

2.3. Catalytic Properties of Pt-Co_3O_4 (n)

The fundamental HER in acidic environment represents an ideal model reaction for investigating the impact of spatial correlation of Pt sites on the catalytic properties of Pt-Co_3O_4 (n) catalysts because the catalytic performance can be explicitly correlated with catalyst's electronic structure. As demonstrated by polarization curves measured in H_2 saturated 0.1 M $HClO_4$ solution, the Pt-Co_3O_4 (n) catalysts exhibit increased apparent activity with increasing Pt content (**Figure 2**a).[8a] The H_2 saturation permits reliable definition of equilibrium potential and determination of overpotential.[17] The electrochemical active surface area (ECSA) normalized specific activity of the Pt-Co_3O_4 (n) catalysts improves with increasing n from 0.01 to 0.06, yet slightly decreases when the n further increases to 0.14 (Figure 2b; Figure S14, Supporting Information). Accordingly, we established the Tafel plots for the Pt-Co_3O_4 (n) catalysts and extracted the exchange current density (j_0) by fitting with the Butler-Volmer equation (Figure 2c). It is demonstrated that the j_0 of the Pt-Co_3O_4 (n) catalysts increases from 0.95, 2.80 to 3.81 mA cm^{-2}_{Pt} with the increasing Pt ratio in Pt-Co_3O_4 (0.01), Pt-Co_3O_4 (0.04), Pt-Co_3O_4 (0.06) and remains at 3.90 mA cm^{-2}_{Pt} for the Pt-Co_3O_4 (0.14) (Table S3, Supporting Information). When the mass of Pt in the catalysts was taken into consideration, a similar mass activity trend of Pt-Co_3O_4 (0.06) > Pt-Co_3O_4 (0.14) > Pt-Co_3O_4 (0.04) > Pt-Co_3O_4 (0.01) can be delivered (Figure 2d). This result suggests that the catalytic performance of Pt-Co_3O_4 (n) catalysts is closely related to the spatial correlation among Pt substitutions in the catalysts. Catalysts with higher spatial correlation of Pt single atoms exhibit significantly promoted HER activity in comparison with the catalyst with mainly isolated Pt single atoms as well as commercial Pt/C catalysts (Figure S15, Supporting Information).

Further, we employed turnover frequency (TOF) as a more accurate assessment of the intrinsic HER activity of Pt-Co_3O_4 (n) in comparison with commercial Pt/C catalysts. At the same Pt loading of ≈10 μg_{Pt} cm^{-2}, the Pt-Co_3O_4 (0.06) catalyst delivers an 8.3-fold higher TOF of 9.41 s^{-1} (at an overpotential of -15 mV) than that of Pt/C (1.13 s^{-1}, which is consistent with literature values[18]), which suggests the enhanced catalytic performance of interactive Pt SACs in comparison with conventional nanoparticle catalysts and other recently reported catalysts (Table S4, Supporting Information). Further, we evaluated the activity of commercial Pt/C catalysts under various Pt loadings that are comparable with the Pt-Co_3O_4 (n) catalysts. The apparent activity of Pt/C catalysts increases with the increase of Pt loading on a glassy carbon electrode (Figure 2e), while due to the

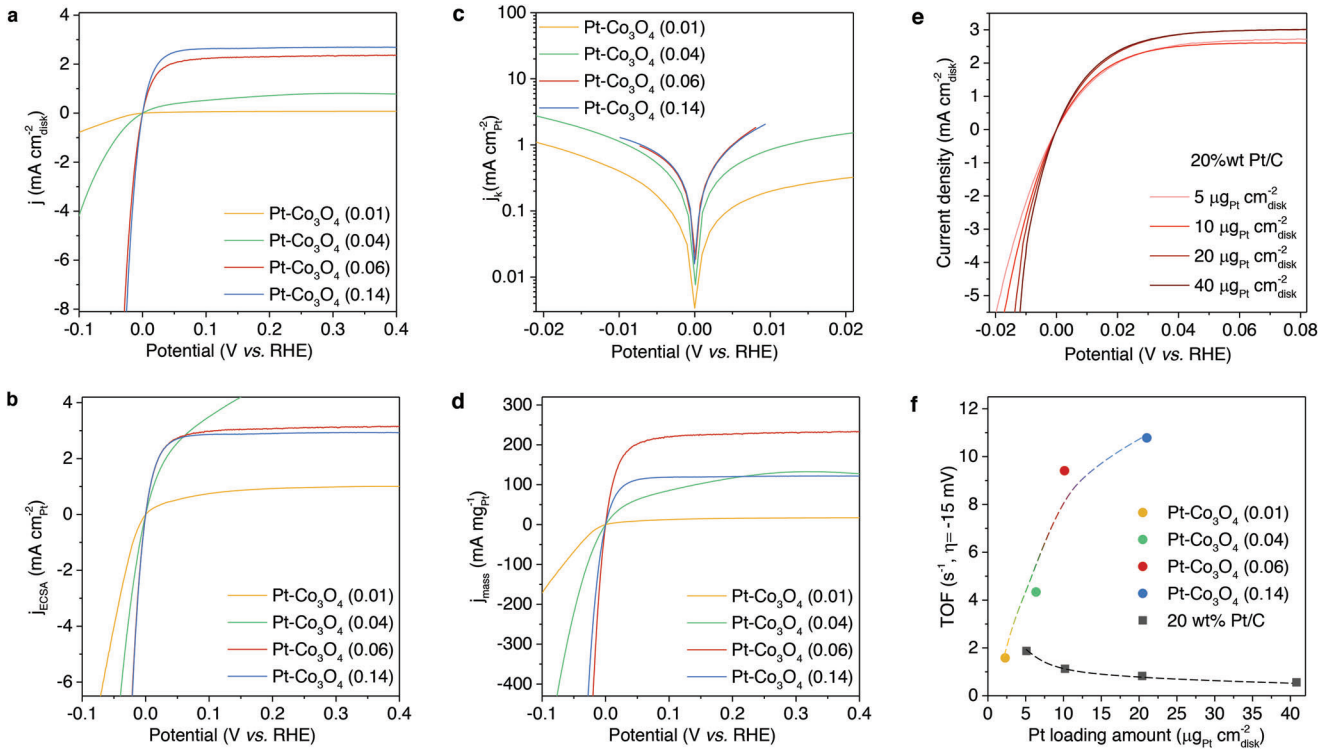

Figure 2. Hydrogen electrocatalytic performance of Pt-Co_3O_4 (n) catalysts. a) Polarization curves on Pt-Co_3O_4 (n) catalysts in H_2-satuated 0.1 M $HClO_4$. b) Specific activity of the Pt-Co_3O_4 (n) catalysts normalized to surface area of Pt sites. c) Tafel plots of the kinetic current density for Pt-Co_3O_4 (n) catalysts. d) Polarization curves normalized to the mass of Pt loaded on the electrodes. e) Polarization curves for Pt/C catalysts with different Pt loadings. f) TOF versus Pt loading for Pt-Co_3O_4 (n) and Pt/C catalysts. The Pt loadings of Pt-Co_3O_4 (n) catalysts were determined by the different Pt mass fractions in various catalysts under the identical catalyst loading of ≈200 $\mu g_{catalyst}$ $cm^{-2}{}_{disk}$. The Pt loadings of Pt/C catalyst were determined by a series of different catalyst loadings on the disk.

mass-transport limitation,[18] the TOF value decreases with increasing Pt loading (Figure 2f). It is interesting to observe an opposite trend of a gradual increase in the TOF value with increasing Pt loading on the Pt-Co_3O_4 (n) catalysts (Figure 2f). This exceptional electrochemical behavior, which is contrary to the widely accepted recognition of mass transport as the critical performance determinant in bulk and nanoparticle Pt catalysts, suggests the distinct electronic structure of Pt single atoms in Pt-Co_3O_4 (n) catalysts originated from fine regulation of site-to-site interactions.

2.4. Structure-Property Relationship of Pt-Co_3O_4 (n) Catalysts

We then explored the quantitative relationship between the correlation degree of Pt sites and the catalytic performance of Pt-Co_3O_4 (n) to explain the abnormal activity trend of Pt-Co_3O_4 (n) hybrids compared with conventional Pt/C. As a result, a nearly identical trend was observed between the specific HER activity and the correlation degree of Pt sites, as the j_0 value of the Pt-Co_3O_4 (n) catalysts increases with the percentage of correlated Pt atoms in these catalysts (**Figure 3**a). On the other hand, the modulated spatial correlation of Pt sites also alters their local coordination environments, which can be unambiguously identified by Pt L_3-edge FT-EXAFS spectra (Table S3, Supporting Information). Interestingly, we observed an identical trend for the correlation between Pt–Pt CN and j_0 values (Figure 3b). Because the Pt–Pt average CN determined by FT-EXAFS fitting can be directly associated with the percentage of correlated Pt sites observed by HRSTEM, their respective relationship with catalytic activity originates from the same physical parameter, namely, the degree of spatial correlation of the interactive Pt sites.

2.5. Structure Modelling of Pt-Co_3O_4 (n) Catalysts

To reveal the origin of unique catalytic behavior of the Pt-Co_3O_4 (n) catalysts in comparison with isolated SACs and nanoparticle catalysts, we performed density functional theory (DFT) computations to investigate the electronic structure of correlated Pt sites with tunable spatial structure. Following the experimental observations, we constructed DFT models by replacing Co_{oct} atom(s) with one Pt atom to represent the Pt single atom catalyst (Pt_1-Co_3O_4) and with 2–4 Pt atoms grouping into various type of "clusters" to represent the correlated Pt substitutions in Co_3O_4 (denoted as Pt_n-Co_3O_4, n = 1–4, Figure S16, Supporting Information). First, we constructed all the possible 11 configurations with Pt substitutions locating at the first and second outermost surfaces. To determine the most stable configurations for models with a certain Pt cluster size, we compared the relative energies of them (**Figure 4**a) and identified the ones with the lowest relative energies and (Figure 4b). Second, based on the most

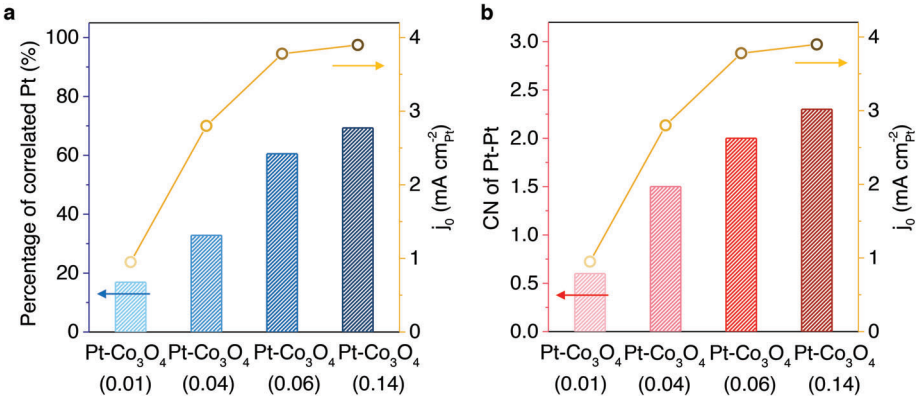

Figure 3. Structure-property relationship of Pt-Co_3O_4 (n) catalysts. a) The relationship between the electrocatalytic activity and the percentage of correlated Pt sites for Pt-Co_3O_4 (n) catalysts. b) The relationship between the specific electrocatalytic activity and CN of second-shell Pt–Pt scattering for Pt-Co_3O_4 (n) catalysts.

stable configurations, we constructed a ternary phase diagram to investigate the thermodynamic stability of the competing phases of Pt_n-Co_3O_4 accommodating different number of interactive Pt atoms. It was found that all the Pt_n-Co_3O_4 configurations were thermodynamically stable against the possible competing phases (Figure 4c).

2.6. Investigation of Electronic Structure

The free energy change of hydrogen adsorption (ΔG_{H^*}, see Methods for details) on different surface Pt adsorption sites was calculated. In total 22 different surface Pt adsorption sites on these four slab models was calculated as shown in **Figure 5**a and

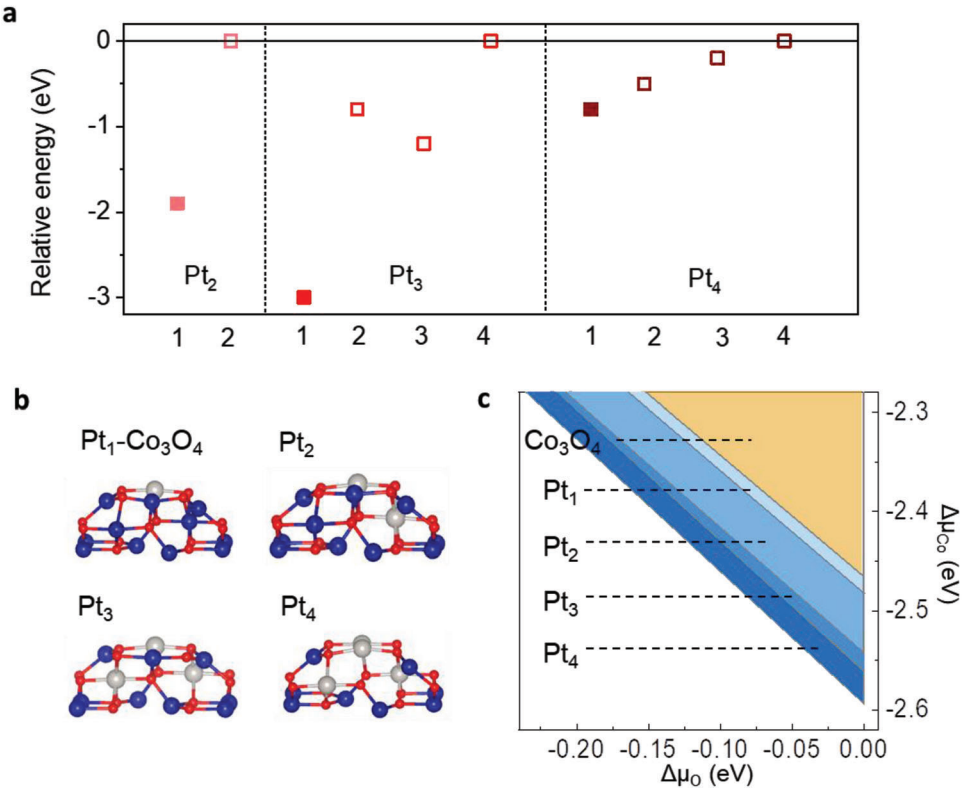

Figure 4. Thermodynamic stabilities of correlated Pt substituted Co_3O_4. a) Calculated relative energies of various configurations for Co_3O_4 models with different Pt cluster sizes (Pt_2–Pt_4). The configuration with the lowest free energy is defined as 0 eV and the relative energies of the other configurations are determined accordingly. b) Structure illustration of Pt-substituted Co_3O_4 with Pt single atom (Pt_1-Co_3O_4) and Pt clusters with different sizes (Pt_n-Co_3O_4, $n = 2$–4). The navy, silver and red spheres represent Co, Pt, and O atoms, respectively. c) The projected ternary phase diagram of the competing phases of Pt_n-Co_3O_4 and Co_3O_4 slabs in the ($\Delta\mu_{Co}$, $\Delta\mu_O$) plane, in which the regions with different blue colors indicate the thermodynamically stable phases.

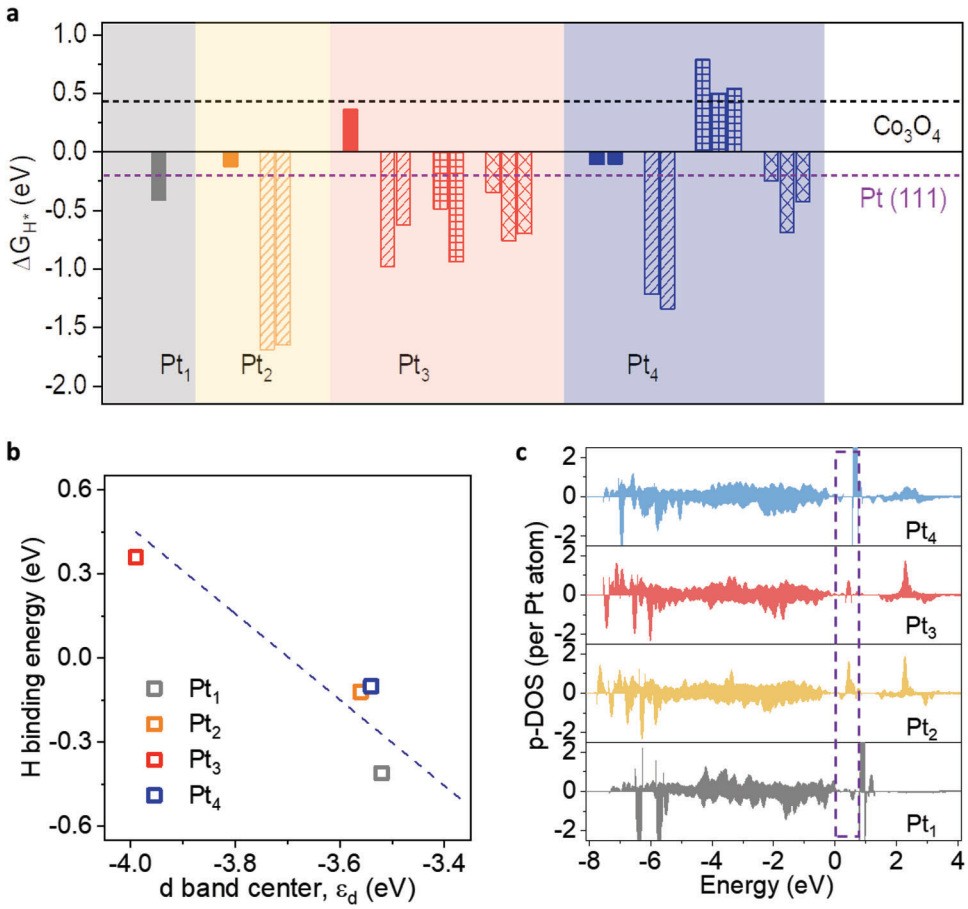

Figure 5. Theoretical investigations of electronic properties of correlated Pt substituted Co_3O_4. a) The calculated hydrogen adsorption free energy changes for various configurations. The solid bars represent the values for the most stable configurations of each Pt cluster size. The black and blue horizontal lines indicate the value on Co_3O_4 and Pt (1 1 1), respectively. b) The relationship between *d*-band center of active sites and hydrogen binding energy on Pt_1 and Pt_2–Pt_4 substituted Co_3O_4. c) Calculated Pt pDOS curves for Pt_1-Co_3O_4 and correlated Pt_2–Pt_4 substituted Co_3O_4.

Figure S17 (Supporting Information). As expected, the values of ΔG_{H^*} vary significantly on different structure configurations. It is indicated that the $|\Delta G_{H^*}|$ values for interactive $Pt_{2\text{-}4}$-Co_3O_4 slabs are much smaller than those of pure Co_3O_4 and Pt_1-Co_3O_4; some are even more optimized than that of Pt (1 1 1).

The smallest ΔG_{H^*} values of −0.12, +0.36, and −0.10 eV were obtained for the surface Pt sites in the most stable Pt_2-, Pt_3-, and Pt_4-Co_3O_4 configurations, respectively (Figure 5a solid bars). This result demonstrates that the well-regulated local Pt–Pt coordination facilitates hydrogen adsorption on the interactive Pt sites. Therefore, the experimental observations that catalysts with more correlated Pt sites exhibit higher intrinsic catalytic activity can be attributed to the favorable electronic structure of spatial correlated Pt substitutions in the Co_3O_4 lattice.

Accordingly, we proposed active sites consisting of central Pt sites and the nearest neighboring Pt and Co_{oct} sites in the Pt_n-Co_3O_4 models. The *d*-band center of the active site can be used to quantitatively elucidate the remarkable catalytic activity of Pt_n-Co_3O_4 catalysts from the perspective of electronic structure. It was found that a largely linear relationship can be established between the hydrogen binding energies and the Pt-Co_{oct} domain's *d*-band centers among different $Pt_{1\text{-}4}$-Co_3O_4 models, while such trend was not found with the active sites consisting of sole Pt sites (Figure 5b; Figure S18, Supporting Information). Based on the d-band center theory proposed by Hammer and Norskov,[19] a linear relationship between the *d*-band centers of the active sites/domain and hydrogen adsorption energies was demonstrated. Therefore, it is determined that the active sites are central Pt sites together with the nearest neighboring Pt and Co_{oct} sites. In addition, the density of states (DOS) analysis shows that the $Pt_{2\text{-}4}$-Co_3O_4 models exhibit additional Pt-5*d* states and a nearly disappeared bandgap, which approaches that of a conductive bulk Pt metal and demonstrates the metal-like behavior of interactive Pt sites (Figure 5c; Figure S19, Supporting Information).[20] Therefore, the combination of theoretical investigations and experimental evaluations demonstrates that the well regulation of site-to-site interactions among Pt sites is critical for boosting catalytic activity on interactive Pt SACs by modifying their electronic structure.

3. Conclusion

In summary, we integrate Pt atomic substitutions in the Co_{oct} sites of cobalt spinel oxide lattice with adjustable spatial

configurations. The Pt sites in a series of Pt-Co_3O_4 (n) catalysts exhibit different degree of spatial correlation and local coordination number as mediated by contents of Pt sites incorporated in the lattice of Co_3O_4. The controllable regulation of spatial structure of Pt sites allows precisely modified *d*-band center of active sites and favorable hydrogen adsorption strength, resulting in enhanced HER electrocatalytic activity of Pt-Co_3O_4 (n) catalysts in comparison with the isolated SACs and nanoparticle catalysts. This work provides a great promise for the rational design of highly efficient interactive SACs by controllably tuning spatial structure of high-density single atoms, which permits precise regulation of geometric and electronic structures of interactive SACs.

4. Experimental Section

Synthesis of Pt-Co_3O_4 (n) Catalysts: The Pt-Co_3O_4 (n) catalysts were synthesized by a similar ion exchange-pyrolysis procedure we reported previously.[21] Typically, Co-based zeolitic imidazolate framework (ZIF-67) nanocubes were first synthesized by a surfactant-mediated method.[22] Afterwards an ion exchange process was conducted on in a 50 mL aqueous solution containing 100 mg of ZIF-67 nanocubes in the presence of platinum precursor. Different addition doses of potassium hexachloroplatinate (IV) (K_2PtCl_6) were dissolved in 10 mL of DI water and added in the ZIF-67 solution under stirring conditions. Three hours later the precipitate was collected and repeatedly washed with ethanol and DI water. After being dried overnight in a vacuum oven at 60 °C, the precipitate was pyrolyzed at 300 °C in air for 4 h. By adding different doses of K_2PtCl_6 from 1.9, 5.8, 9.7, to 19.4 mg, a series of Pt-Co_3O_4 (n) with different Pt contents could be obtained. Under the stoichiometry of $Pt_nCo_{3-n}O_4$, the n values were determined by ICP-MS to be 0.01, 0.04, 0.06, and 0.14, for simplicity, the catalysts were denoted as Pt-Co_3O_4 (0.01), Pt-Co_3O_4 (0.04), Pt-Co_3O_4 (0.06), and Pt-Co_3O_4 (0.14), respectively.

HRSTEM Imaging and Simulations: HAADF-STEM images were recorded using a Thermo Fisher Spectra 300 electron microscope operated at 300 kV and equipped with a probe corrector. The projected Z^2-map and probe profile simulations were carried out by using the QSTEM program[23] with different supercell configurations. For the 3D probe profile simulation, a focal series from −30 to 30 nm with an interval of 1 nm was conducted, using a convergence angle of 30 mrad, third order spherical aberration (C3) of 1 µm and fifth order spherical aberration (C5) of 300 µm. After flat-field correction and background subtraction, the position searching, refining and labelling of the projected Pt sites with brighter contrast in the HRSTEM image were carried out using CalAtom software[24] with a Multiple-Ellipse-Fitting (MEF) method.[25] Instead of directly locating individual Pt sites within the cationic sublattice of host structure, identifying "projected Pt clusters" from as-labelled Pt doped brighter atomic columns with an intensity penalty (>70%) offers a sensible evaluation of 3D clustering probability of Pt sites over ultrathin regions. Based on the simulated 3D probe profile using imaging parameters and aberration coefficients similar to experimental imaging conditions, it was clear that the identified Pt atoms at the cationic sites were most likely within a few unit cells in height and could be regarded as correlated sites with short-range order.

DFT Calculations: DFT calculations were carried out using the Vienna ab-initio Simulation Package (VASP).[26] The exchange-correlation interaction was described by generalized gradient approximation (GGA) with the Perdew-Burke-Ernzerhof (PBE) functional.[27] The DFT-TS method of Grimme was employed to treat the VDW interaction. Denser 8 × 8 × 2 K-points were used for the DOS calculations. In an acidic solution, a simple method was used to compute the free energy based on the hydrogen adsorption strength, as in previous calculations:[28]

$$\Delta G_H* = \Delta E_H + 0.24\ \text{eV} \quad (1)$$

$$\Delta E_H = E_{total} - 1/2E_{H2} - E_s \quad (2)$$

where E_{total}, E_{H2}, and E_s are the energies of the whole system, hydrogen and substrate, respectively. The GGA+U calculations were performed using the model proposed based on the TEM images with the U_{eff} (U_{eff} = Coulomb U – exchange J) values of 4.4, 6.7, 3.2 eV for Co^{2+}, Co^{3+}, Pt, respectively.[29] For the plane-wave expansion, a kinetic energy cut-off of 600 eV was used after testing a series of different cut-off energies. The force and energy convergence tolerance values were set to be 0.01 eV $Å^{-1}$ and 10^{-5} eV, respectively. A Gaussian smearing of 0.1 eV was applied during the geometry optimization, while for the accurate calculation of the density of states a tetrahedron method with Blöchl correction was employed. The K-points were set to be 2 × 2 × 1 for the unit cells. All periodic slabs had a vacuum spacing of at least 15 Å. The (1 1 0) facet of Co_3O_4 was selected because it is composed mainly of Co_{oct} cations, which had been proved by experimental studies.[30] The structural model of Co_3O_4 (1 1 0) facet contains three Co-O layers (88 atoms), with a supercell size of a = 16.80 Å, b = 11.88 Å, c = 17.97 Å, $\alpha = \beta = \gamma = 90°$. In calculations, the bottom layer was kept fixed, whereas the rest of atoms were allowed to relax.

Supporting Information

Supporting Information is available from the Wiley Online Library or from the author.

Acknowledgements

C.Y. and J.S. contributed equally to this work. This work was financially supported by the Australian Research Council through the Discovery and Linkage Project programs (FL170100154, DP220102596, DP190103472, and LP210301397), the Australian Research Council Discovery Early Career Researcher Award (DE230101011).

Open access publishing facilitated by The University of Adelaide, as part of the Wiley - The University of Adelaide agreement via the Council of Australian University Librarians.

Conflict of Interest

The authors declare no conflict of interest.

Data Availability Statement

The data that support the findings of this study are available from the corresponding author upon reasonable request.

Keywords

electrocatalysis, electronic structure, single atom catalysts, site-to-site interaction, spatial structure

Received: July 10, 2023
Revised: September 25, 2023
Published online: October 20, 2023

[1] a) L. Liu, A. Corma, *Chem. Rev.* **2018**, *118*, 4981; b) S. Mitchell, R. Qin, N. Zheng, J. Pérez-Ramírez, *Nat. Nanotechnol.* **2021**, *16*, 129.
[2] a) L. Lin, W. Zhou, R. Gao, S. Yao, X. Zhang, W. Xu, S. Zheng, Z. Jiang, Q. Yu, Y.-W. Li, C. Shi, X.-D. Wen, D. Ma, *Nature* **2017**, *544*, 80; b) E. Vorobyeva, E. Fako, Z. Chen, S. M. Collins, D. Johnstone, P. A. Midgley, R. Hauert, O. V. Safonova, G. Vilé, N. López, S. Mitchell, J. Pérez-Ramírez, *Angew. Chem., Int. Ed.* **2019**, *58*, 8724.

[3] M. Peng, C. Dong, R. Gao, D. Xiao, H. Liu, D. Ma, *ACS Cent. Sci.* **2021**, *7*, 262.
[4] a) J. Yang, W.-H. Li, S. Tan, K. Xu, Y. Wang, D. Wang, Y. Li, *Angew. Chem., Int. Ed.* **2021**, *60*, 19085; b) X. Cui, W. Li, P. Ryabchuk, K. Junge, M. Beller, *Nat. Catal.* **2018**, *1*, 385.
[5] H. Li, L. Wang, Y. Dai, Z. Pu, Z. Lao, Y. Chen, M. Wang, X. Zheng, J. Zhu, W. Zhang, R. Si, C. Ma, J. Zeng, *Nat. Nanotechnol.* **2018**, *13*, 411.
[6] a) W. Wan, Y. Zhao, S. Wei, C. A. Triana, J. Li, A. Arcifa, C. S. Allen, R. Cao, G. R. Patzke, *Nat. Commun.* **2021**, *12*, 5589; b) S. Tian, B. Wang, W. Gong, Z. He, Q. Xu, W. Chen, Q. Zhang, Y. Zhu, J. Yang, Q. Fu, C. Chen, Y. Bu, L. Gu, X. Sun, H. Zhao, D. Wang, Y. Li, *Nat. Commun.* **2021**, *12*, 3181.
[7] C. Lin, J.-L. Li, X. Li, S. Yang, W. Luo, Y. Zhang, S.-H. Kim, D.-H. Kim, S. S. Shinde, Y.-F. Li, Z.-P. Liu, Z. Jiang, J.-H. Lee, *Nat. Catal.* **2021**, *4*, 1012.
[8] a) J. Shan, C. Ye, C. Zhu, J. Dong, W. Xu, L. Chen, Y. Jiao, Y. Jiang, L. Song, Y. Zhang, M. Jaroniec, Y. Zhu, Y. Zheng, S.-Z. Qiao, *J. Am. Chem. Soc.* **2022**, *144*, 23214; b) J. Shan, C. Ye, S. Chen, T. Sun, Y. Jiao, L. Liu, C. Zhu, L. Song, Y. Han, M. Jaroniec, Y. Zhu, Y. Zheng, S.-Z. Qiao, *J. Am. Chem. Soc.* **2021**, *143*, 5201.
[9] a) Z. Jin, P. Li, Y. Meng, Z. Fang, D. Xiao, G. Yu, *Nat. Catal.* **2021**, *4*, 615; b) Q. Wang, X. Huang, Z. L. Zhao, M. Wang, B. Xiang, J. Li, Z. Feng, H. Xu, M. Gu, *J. Am. Chem. Soc.* **2020**, *142*, 7425; c) X. Meng, C. Ma, L. Jiang, R. Si, X. Meng, Y. Tu, L. Yu, X. Bao, D. Deng, *Angew. Chem., Int. Ed.* **2020**, *59*, 10502.
[10] C. Chu, D. Huang, S. Gupta, S. Weon, J. Niu, E. Stavitski, C. Muhich, J.-H. Kim, *Nat. Commun.* **2021**, *12*, 5179.
[11] J. Shan, C. Ye, Y. Jiang, M. Jaroniec, Y. Zheng, S.-Z. Qiao, *Sci. Adv.* **2022**, *8*, eabo0762.
[12] B. Hammer, J. K. Norskov, *Adv. Catal.* **2000**, *45*, 71.
[13] a) J. Kim, P.-C. Shih, K.-C. Tsao, Y.-T. Pan, X. Yin, C.-J. Sun, H. Yang, *J. Am. Chem. Soc.* **2017**, *139*, 12076; b) L. Jiao, E. Liu, S. Hwang, S. Mukerjee, Q. Jia, *ACS Catal.* **2021**, *11*, 8165.
[14] J. Shan, J. Liao, C. Ye, J. Dong, Y. Zheng, S.-Z. Qiao, *Angew. Chem., Int. Ed.* **2022**, *61*, 202213412.
[15] Y. Fang, Q. Zhang, H. Zhang, X. Li, W. Chen, J. Xu, H. Shen, J. Yang, C. Pan, Y. Zhu, J. Wang, Z. Luo, L. Wang, X. Bai, F. Song, L. Zhang, Y. Guo, *Angew. Chem.* **2022**, *134*, 202212273.
[16] J. Preudhomme, P. Tarte, *Spectrochim. Acta, Part A* **1971**, *27*, 1817.
[17] X. Tian, P. Zhao, W. Sheng, *Adv. Mater.* **2019**, *31*, 1808066.
[18] J. N. Hansen, H. Prats, K. K. Toudahl, N. Mørch Secher, K. Chan, J. Kibsgaard, I. Chorkendorff, *ACS Energy Lett.* **2021**, *6*, 1175.
[19] M. Mavrikakis, B. Hammer, J. K. Nørskov, *Phys. Rev. Lett.* **1998**, *81*, 2819.
[20] W. S. Choi, M. F. Chisholm, D. J. Singh, T. Choi, G. E. Jellison, H. N. Lee, *Nat. Commun.* **2012**, *3*, 689.
[21] J. Shan, C. Ye, S. Chen, T. Sun, Y. Jiao, L. Liu, C. Zhu, L. Song, Y. Han, M. Jaroniec, Y. Zhu, Y. Zheng, S.-Z. Qiao, *J. Am. Chem. Soc.* **2021**, *143*, 5201.
[22] H. Hu, B. Y. Guan, X. W. Lou, *Chem* **2016**, *1*, 102.
[23] C. T. Koch, *Ph.D. Thesis*, Arizona State University, United States **2002**, Determination of core structure periodicity and point defect density along dislocations.
[24] Q. Zhang, L. Y. Zhang, C. H. Jin, Y. M. Wang, F. Lin, *Ultramicroscopy* **2019**, *202*, 114.
[25] Q. Zhang, C. H. Jin, H. T. Xu, L. Y. Zhang, X. B. Ren, Y. Ouyang, X. J. Wang, X. J. Yue, F. Lin, *Micron* **2018**, *113*, 99.
[26] a) G. Kresse, J. Furthmüller, *Phys. Rev. B* **1996**, *54*, 11169; b) G. Kresse, J. Furthmüller, *Comp. Mater. Sci.* **1996**, *6*, 15.
[27] J. P. Perdew, K. Burke, M. Ernzerhof, *Phys. Rev. Lett.* **1996**, *77*, 3865.
[28] J. K. Nørskov, T. Bligaard, A. Logadottir, J. R. Kitchin, J. G. Chen, S. Pandelov, U. Stimming, *J. Electrochem. Soc.* **2005**, *152*, J23.
[29] a) J. Chen, X. Wu, A. Selloni, *Phys. Rev. B* **2011**, *83*, 245204; b) G. Lan, J. Song, Z. Yang, *J. Alloys Compd.* **2018**, *749*, 909.
[30] X. Xie, Y. Li, Z. Q. Liu, M. Haruta, W. Shen, *Nature* **2009**, *458*, 746.